Environmental Science & Technology

pubs.acs.org/est

Article

# Selective Adsorption and Photocatalytic Degradation of Extracellular Antibiotic Resistance Genes by Molecularly-Imprinted Graphitic Carbon Nitride

Qingbin Yuan,[#] Danning Zhang,[#] Pingfeng Yu,[*] Ruonan Sun, Hassan Javed, Gang Wu, and Pedro J. J. Alvarez[*]

Cite This: *Environ. Sci. Technol.* 2020, 54, 4621−4630

Read Online

ACCESS | Metrics & More | Article Recommendations | Supporting Information

**ABSTRACT:** There is a growing need to mitigate the discharge of extracellular antibiotic resistance genes (ARGs) from municipal wastewater treatment systems. Here, molecularly-imprinted graphitic carbon nitride (MIP-$C_3N_4$) nanosheets were synthesized for selective photocatalytic degradation of a plasmid-encoded ARG ($bla_{NDM-1}$, coding for multidrug resistance New Delhi metallo-$\beta$-lactamase-1) in secondary effluent. Molecular imprinting with guanine enhanced ARG adsorption, which improved the utilization of photogenerated oxidizing species to degrade $bla_{NDM-1}$ rather than being scavenged by background nontarget constituents. Consequently, photocatalytic removal of $bla_{NDM-1}$ in secondary effluent with MIP-$C_3N_4$ ($k$ = 0.111 ± 0.028 $min^{-1}$) was 37 times faster than with bare graphitic carbon nitride ($k$ = 0.003 ± 0.001 $min^{-1}$) under UVA irradiation (365 nm, 3.64 × $10^{-6}$ Einstein/L·s). MIP-$C_3N_4$ can efficiently catalyze the fragmentation of $bla_{NDM-1}$, which decreased the potential for ARG repair by transformed bacteria. Molecular imprinting also changed the primary degradation pathway; electron holes ($h^+$) were the predominant oxidizing species responsible for $bla_{NDM-1}$ removal with MIP-$C_3N_4$ versus free radicals (i.e., ·OH and $O_2^-$) for coated but nonimprinted $C_3N_4$. Overall, MIP-$C_3N_4$ efficiently removed $bla_{NDM-1}$ from secondary effluent, demonstrating the potential for molecular imprinting to enhance the selectivity and efficacy of photocatalytic processes to mitigate dissemination of antibiotic resistance from sewage treatment systems.

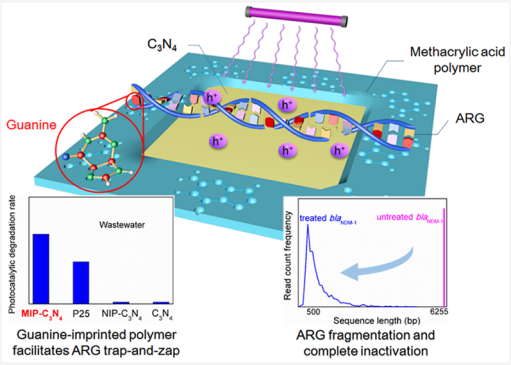


## INTRODUCTION

The global spread of antibiotic resistance genes (ARGs) and their potential assimilation by pathogenic bacteria constitutes a growing threat to public health.[1] Some municipal wastewater treatment plants (WWTPs) may serve as breeding grounds and point sources of ARGs due to selective pressure by the presence of sublethal levels of antibiotics and high bacterial densities that facilitate horizontal gene transfer.[2] Conventional WWTP disinfection processes (e.g., chlorination and UV radiation), though moderately effective in removing antibiotic resistant bacteria,[3,4] are relatively ineffective in removing ARGs.[5] Accordingly, extracellular ARGs can persist, transform bacteria, and propagate with their new hosts in the receiving water.[6,7] Moreover, residual chlorine reaching the receiving environment may be diluted to sublethal levels that increase the permeability of indigenous bacteria cells and enhance ARG transfer,[8] and UV-inactivated ARGs may be reactivated by transformed bacteria.[8,9] Therefore, reliable and sustainable disinfection processes are needed for removing ARGs during municipal wastewater treatment.

Photocatalysis has received significant attention as a potentially eco-friendly disinfection and advanced oxidation process since it does not require continuous addition of chemical disinfecting agents. The photogenerated reactive oxygen species (ROS) can inactivate ARGs by damaging nucleotides.[10,11] Graphitic carbon nitride ($C_3N_4$) is an earth-abundant and metal-free photocatalyst[12] that can be easily modified to achieve high photocatalytic efficiency.[13] For example, edge-functionalization of $C_3N_4$ with electron-withdrawing groups (e.g., carboxyl groups) may improve charge separation and ROS generation.[14] However, degradation of ARGs by pristine or modified $C_3N_4$ can be adversely affected in WWTP effluent, where soluble microbial product (SMPs)[15] and natural organic matter (NOM) compete with less abundant target contaminants (or ARGs in this case) for photogenerated ROS.[16] This challenge underscores the need to develop novel photocatalysts that are capable of selectively degrading extracellular ARGs.

Received: November 18, 2019
Revised: March 5, 2020
Accepted: March 9, 2020
Published: March 9, 2020

**Scheme 1. Schematic Diagram of Three-Step Fabrication of MIP-$C_3N_4$**[a]

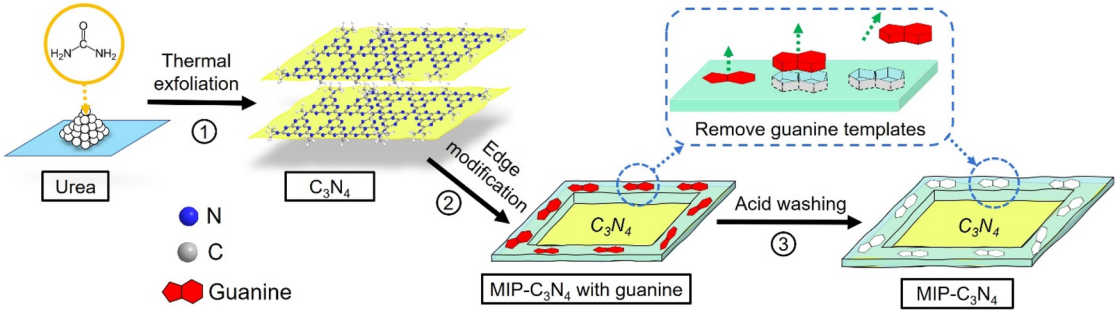


[a]Fabrication of graphitic $C_3N_4$ through thermal exfoliation of recrystallized urea followed by edge polymerization of MIP and subsequent acid washing.

Molecular imprinting is a technique to impart high selectivity to polymers toward specific pollutants by creating binding sites that are complementary in size and shape to the templates, which results in specific recognition of target molecules.[17] Conjugating molecularly-imprinted polymerwith photocatalysts can improve the efficiency of photocatalytic processes by enhancing the selectivity of the MIP−photocatalyst composite toward target contaminants.[18] Compared with other WWTP effluent constituents (e.g., SMPs and NOM), ARGs as DNA are characterized by their high content of nucleotides (i.e., adenine, guanine, cytosine, and thymine).[19] Therefore, previous researchers have used molecular imprinting of guanine for developing DNA sensors.[20] Using similar principles, molecular imprinting of nucleotides may create selective recognition sites on the catalyst surface,[21−23] enabling the catalyst to selectively entrap extracellular ARGs near photocatalytic sites for more efficient degradation. Improved contact between ARGs and catalyst would enhance the utilization of photogenerated ROS by ARGs rather than scavenging by nontargeted constituents (a.k.a., the "trap and zap" strategy[24,25]).

Our driving hypothesis is that selective DNA capture and photocatalytic treatment improves ARG fragmentation and inactivation efficiency during photocatalytic effluent polishing. As widely reported by previous research,[26,27] fragmented ARGs permanently loose their ability to confer antibiotic resistance. This represents a significant potential advantage over traditional disinfection techniques (e.g., UV and chlorination), which cause nucleotide lesions that may be repaired by transformed bacteria[5,28,29] and do not eliminate the risk of ARG repair after treatment in receiving environments.

Here, we report a novel guanine-imprinted $C_3N_4$-based photocatalyst and demonstrate its effectiveness to remove ARGs in the presence of coexisting ROS-scavenging water constituents. Photocatalytic degradation of New Delhi metallo-$\beta$-lactamase-1 ($bla_{NDM-1}$), a multidrug-resistant gene,[30,31] by MIP-$C_3N_4$ was tested in the presence of different common organic compounds (i.e., peptone, sucrose, and humic acid) and in secondary effluent from a municipal wastewater treatment plant. The photocatalytic mechanism was investigated through ROS scavenging tests and DNA fragment characterization. Photocatalytic performance in secondary effluent, where ROS scavengers are abundant, was benchmarked against both a commercial $TiO_2$ photocatalyst and unprinted $C_3N_4$ as proof-of-concept that molecular imprinting can enhance the selectivity and efficacy of photocatalytic processes to degrade extracellular ARGs (eARGs) in complex matrices.

## MATERIALS AND METHODS

**Chemicals.** Urea (≥97%), potassium permanganate ($KMnO_4$, ≥99.0%), sulfoxide chloride ($SOCl_2$, ≥99.7%), chloroform (≥99%), tetrahydrofuran (THF, ≥99%), 4-(dimethylamino) pyridine (4-DMAP, ≥99%), allyl alcohol (≥99%), *N*,*N*-dimethylformamide (≥99.8%), triethylamine (≥99%), guanine (≥98%), 2,2′-azobis(2-methylpropionitrile) (AIBN, ≥98%), acetonitrile (≥99%), toluene (≥99%), methacrylic acid (MAA, ≥99%), ethylene glycol dimethacrylate (EGDMA, ≥98%), L-histidine (≥99%), catalase from bovine liver, superoxide dismutase (SOD), ammonium oxalate (≥99%), and sodium hydroxide (≥99%) were purchased from Sigma-Aldrich and used as received. Suwannee river natural organic matter (NOM) was purchased from International Humic Substances Society (IHSS). Hydrochloric acid (≥36.5%), sulfuric acid (≥98%), and absolute ethanol were purchased from Millipore-Sigma.

**Synthesis of Graphitic $C_3N_4$ Nanosheets and Modification with a Vinyl Group.** Molecularly-imprinted $C_3N_4$ (MIP-$C_3N_4$) was fabricated through a facile three-step strategy (Scheme 1). Urea was used as a precursor to synthesize graphitic $C_3N_4$ via thermal exfoliation.[32−34] Briefly, urea was recrystallized from aqueous urea solution (0.5 g/mL) heated at 80 °C for 24 h, then calcinated in the air at a ramp rate of 2.4 °C/min for 4 h, and maintained at 550 °C for another 2 h in a tube furnace (STF 1200, Across International). The light-yellow product was agitated and collected.

Since the imprinted polymer must be attached without occluding photocatalytic sites, the as-obtained $C_3N_4$ was partially oxidized to carboxylic $C_3N_4$($C_3N_4$−COOH) through a modified Hummer's method (Supporting Information),[13,35] which ensures carboxylation of mainly $C_3N_4$ nanosheet edges.[14] The carboxylic groups were then substituted by vinyl groups, providing reaction sites for further polymerization with MIP;[20] this facilitates polymer coating primarily of nanosheet edges without significantly occluding the photocatalytic surface. Briefly, $C_3N_4$−COOH (200 mg) was suspended in a mixture of $SOCl_2$ (30 mL) and chloroform (10 mL). The $C_3N_4$−COOH suspension was then refluxed for 24 h at 60 °C. The precipitates from the above reaction were washed with tetrahydrofuran (THF) and transferred into a mixed solution of THF (30 mL) and triethylamine (8.4 mL). To this solution, 0.25 g of 4-DMAP and 1.16 g of ally alcohol were added. The solution was refluxed at 60 °C for 24 h. The


https://dx.doi.org/10.1021/acs.est.9b06926
Environ. Sci. Technol. 2020, 54, 4621−4630

white precipitate was harvested by centrifugation and washed thoroughly with THF. $C_3N_4$ modified with vinyl groups ($C_3N_4$—CH=$CH_2$) was then obtained as precipitate through vacuum drying under 40 °C overnight.

**Synthesis of Molecularly-Imprinted $C_3N_4$.** MIP-$C_3N_4$ was prepared by selective polymerization of methacrylic acid (MAA) with the vinyl groups on the edge of $C_3N_4$—CH=$CH_2$.[36,37] In brief, $C_3N_4$—CH=$CH_2$ (100 mg) was dispersed in a mixture of acetonitrile (60 mL) and toluene (10 mL). The dispersion was then purged with $N_2$ for 30 min. To the $N_2$-saturated dispersion, guanine (90 mg) and MAA (86 μL) were added as template molecule and functional monomer, respectively. After another 30 min of stirring, the cross-linker (EGDMA, 500 μL) and initiator (AIBN, 40 mg) were added. The solution was then transferred into an airtight vial with the cover sealed. The reaction vial was placed in an oil bath and heated at 70 °C for 12 h. The product was collected and washed with ethanol thoroughly to remove possible impurities. The template molecules (guanine) were removed by washing with 1 M HCl. The product was further washed with ethanol until the pH reached neutral. MIP-$C_3N_4$ was obtained by vacuum drying the product under 40 °C overnight. The control (nonmolecularly-imprinted (NIP-$C_3N_4$)) sample was fabricated following the same procedure, only without adding guanine.

**Characterization of MIP-$C_3N_4$.** MIP-$C_3N_4$ was characterized in terms of morphology, crystal structure, specific surface area, functional groups, and surface elements. Functional groups were characterized using FTIR (Fourier transform infrared) microscope (Nicolet iS50 FTIR, Thermo Scientific) scanning from 4000 to 400 $cm^{-1}$ in a KBr tablet. The phase information of $C_3N_4$ was obtained from powder X-ray diffraction (XRD, Rigaku DMAX) with Cu K$\alpha$ radiation ($\lambda$ = 1.54178 Å). The specific surface area was measured using a Brunauer−Emmett−Teller (BET) surface analyzer (Autosorb-3B, Quantachrome Instruments). The morphology was observed with an environmental scanning electron microscope (ESEM, FEI Quanta 400F) with high voltage (20 kV) under high vacuum mode (chamber pressure of $1.45 \times 10^{-4}$ Pa). Transmission electron microscopy (TEM) images and high-resolution TEM analyses were performed by using a JEOL-2010 TEM with an acceleration voltage of 200 kV. Surface chemistry was analyzed by X-ray photoelectron spectroscopy (XPS) equipped with a 100 μm X-ray beam with a takeoff angle of 45° (PHI Quantera SXM). The pass energy was 140 eV for the survey and 26 eV for the high-resolution elemental analysis. The thickness of MIP-$C_3N_4$ was examined by atomic force microscopy (AFM, Park NX20, Park system) in tapping mode. The optical properties were characterized by ultraviolet diffuse reflectance spectra (UV-DRS) using a UV−vis spectrophotometer (UV-2450, Shimadzu, Japan) and confocal Raman microscopy/spectrometer system (Invia Reflex, Renishaw, U.K.).

**Photocatalytic ARG Degradation Tests.** $bla_{NDM-1}$ harbored by an engineered plasmid pET-29a(+) with a total length of 6255 bp was selected as the target ARG. The details of the plasmid are given in Figure S1.[18] A photoreactor (LZC-4V, Luzchem Research Inc.) was used for batch scale photocatalytic tests. Six UVA lamps (365 nm irradiation, 8W, FB8L-B) were installed in the reactor, providing a total light intensity of $3.64 \times 10^{-6}$ Einstein/L/s. The catalyst (5 mg) was dispersed in a 10 mL solution containing $10^9$−$10^{10}$ copies/mL $bla_{NDM-1}$ at the beginning of the photoreaction. The concentration of catalyst used was within the range reported by previous research on photocatalytic removal of ARGs.[38−40] This suspension was stirred and equilibrated for 2 h, and the concentration of $bla_{NDM-1}$ was adjusted to $10^9$−$10^{10}$ copies/mL before irradiation. Aliquots (200 μL) were taken after predetermined intervals of irradiation time for further quantification, and the catalysts were removed by centrifugation. Selectivity tests were conducted in the presence of three common wastewater constituents with different chemical structures and reactivity at representative concentrations[41−43] (i.e., 50 mg/L peptone, 50 mg/L sucrose, and 10 mg/L humic acid) and in secondary wastewater treatment plant effluent (Table S1, total organic carbon (TOC) = 16.1 mg/L) to assess ARG removal efficiency under realistic treatment conditions. To determine the adsorption isotherm, 0.5 mg/mL catalyst dispersion was prepared in which the $bla_{NDM-1}$ concentration was set to a range from $10^9$ to $10^{10}$ copies/mL. These dispersions were stirred vigorously for 24 h to reach adsorption equilibrium.

**ROS Scavenging Tests.** Photocatalytic degradation of $bla_{NDM-1}$ was also evaluated in the presence of various ROS and electron hole ($h^+$) scavengers to determine the primary oxidant(s). These tests were conducted in DI water to avoid confounding effects by organic compounds in secondary effluent. The scavengers utilized include 1 mM isopropanol (IPA) for ·OH, 50 kU/L superoxide dismutase (SOD) for $O_2^{\cdot-}$, 1 mM L-histidine for $^1O_2$, 200 U/mL catalase for $H_2O_2$, and 10 mM ammonium oxalate (AO) for $h^+$.[25,44] The photoactivity inhibition level by each scavenger was calculated using following equation (eq 1).

$$\text{photoactivity inhibition level} = (1 - k_{\text{scavenger}}/k_{\text{control}}) \times 100\% \quad (1)$$

where $k_{\text{scavenger}}$ and $k_{\text{control}}$ represent photocatalytic reaction rate constants with and without the addition of specific scavengers.

The presence of ROS was verified by electron spin resonance (ESR) signals of paramagnetic species spin-trapped with 3,4-dihydro-2-methyl-1,1-dimethylethyl ester-2*H*-pyrrole-2-carboxylic acid-1-oxide (BMPO); the ESR spectra were obtained using a Bruker EMX ESR spectrometer at room temperature.

**DNA Biomarker Quantification and Characterization of Treated DNA.** The abundance of the $bla_{NDM-1}$ gene was quantified by the qPCR process using primer sets (forward primer 5′-CGC AGC TTG TCG GCC ATG-3′ and reverse primer 5′-GGA ATT GCC CAA TAT TAT GC-3′; amplicon size: 807 bp),[45] with details presented in the Supporting Information. Treated $bla_{NDM-1}$ samples were further analyzed by Nanopore Rapid Barcoding Sequencing for fragment characterization. In detail, the treated $bla_{NDM-1}$ (100 ng) was barcoded using the fast barcoded kit (SQK-RBK004) and then characterized with MinKNOW, analyzing the length distribution of DNA fragments using the accompanying EPI2ME platform. The melting curve of the treated $bla_{NDM-1}$ sample was measured on a CFX 96 Real-time System (BIO-RAD, U.S.). The UV−vis adsorption spectrum of treated $bla_{NDM-1}$ after photocatalytic treatment was examined by a Nanodrop 1000 Spectrometer (Thermo Fisher Scientific, U.S.).

**Oligonucleotide Adsorption and Photocatalytic Degradation Tests.** Four oligonucleotides with different guanine contents were tested to assess the selectivity of MIP-$C_3N_4$ toward guanine containing compounds. G0 (5′-CCCA-CCCACCCACCCAAA-3′), G1 (5′-GCCACCCACCCA-


https://dx.doi.org/10.1021/acs.est.9b06926
Environ. Sci. Technol. 2020, 54, 4621−4630

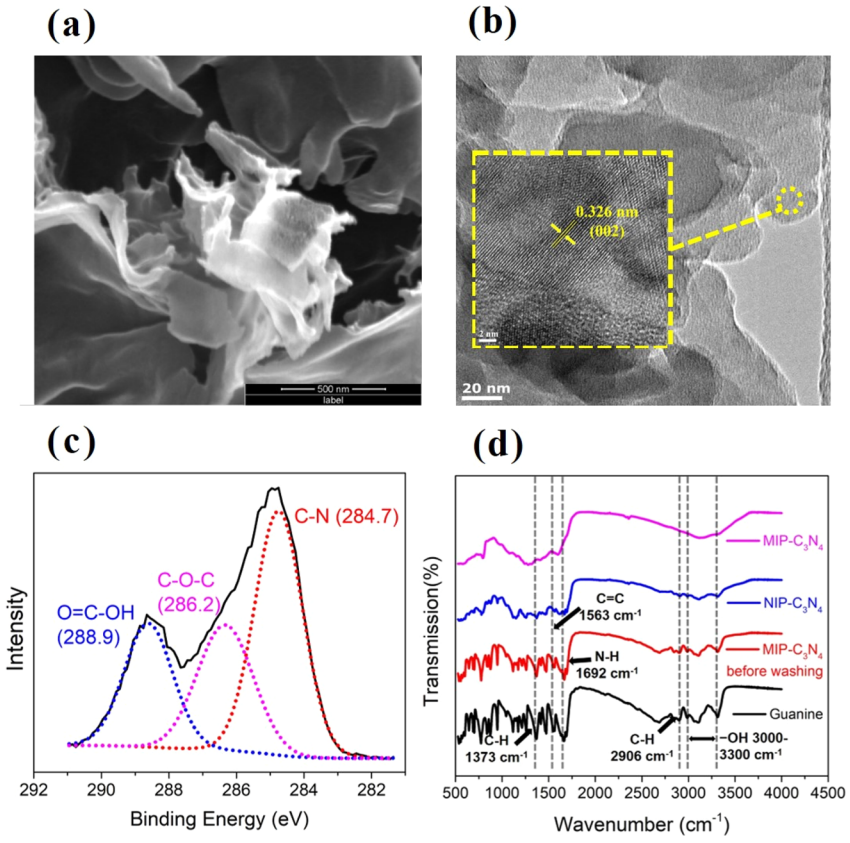


**Figure 1.** Characterization of MIP-$C_3N_4$. (a) SEM images of the MIP-$C_3N_4$ mesoporous structure. (b) HR-TEM images of the magnification of the MIP-$C_3N_4$ edge illustrating the nanosheet structure of and the (002) crystallographic plane of $C_3N_4$. (c) XPS spectra of MIP-$C_3N_4$ depicting that the polymer matrix (288.9 and 286.2 eV) was anchored onto $C_3N_4$ (284.7 eV). (d) FTIR spectra of guanine, MIP-$C_3N_4$ before washing, NIP-$C_3N_4$, and MIP-$C_3N_4$, indicating that guanine was successfully imprinted into the polymer matrix and subsequently removed by acid washing.

CCCAAA-3′), G2 (5′-CCCACCCACCGGCCCAAA-3′), and G3 (5′-CGCACCCACCGGCCCAAA-3′) contain zero, one, two, and three guanines, respectively. 2 mL of oligonucleotide suspension containing G0, G1, G2, or G3 at 50 ng/$\mu$L was spiked with catalyst to achieve a final concentration of 2000 mg/L, which was shaken for 2 h under dark conditions. Aliquots (50 $\mu$L) were taken every half hour, and the catalysts were returned to the above solution after centrifugation. The saturated catalysts were then moved to the photocatalytic reactor, with 2 mL of fresh oligonucleotide suspension (50 ng/$\mu$L) spiked in before irradiation. Aliquots (50 $\mu$L) were taken after predetermined intervals of irradiation time for further quantification, and the catalysts were returned by centrifugation. The concentration of residual oligonucleotides was determined using a Nanodrop 1000 Spectrometer at 260 nm.

**Catalyst Stability Tests.** The stability of MIP-$C_3N_4$ photoactivity was investigated through repeated usage (10 cycles) in deionized water and secondary effluent and compared with that of P25 $TiO_2$. The catalysts were collected and dried after each cycle. MIP-$C_3N_4$ was characterized by SEM and FTIR analysis initially and after the 10th cycle to discern possible morphological and surface chemistry changes.

**Statistical Analysis.** The Student's $t$ test (two-tailed) was used to determine the significance of the differences between treatments. Differences were considered to be significant at the 95% confidence level ($p < 0.05$) and highly significant at the 99% confidence level ($p < 0.01$).

## RESULTS AND DISCUSSION

**Synthesis of Guanine Imprinted Graphitic $C_3N_4$.** Molecular imprinting was used to address one major common limitation of photocatalytic treatment: inefficiency associated with the scavenging of the oxidation capacity by nontarget water constituents.[46,47] SEM images showed a mesoporous structure for MIP-$C_3N_4$ (Figure 1a), and the HR-TEM image depicts the nanosheet structure of the graphitic $C_3N_4$ building blocks (Figure 1b). An interplanar spacing of 0.326 nm was observed, corresponding to the (002) crystallographic plane of $C_3N_4$ (inset of Figure 1b). AFM measurements indicate that the thickness of MIP-$C_3N_4$ was 5 nm (Figure S2). Two new peaks at 288.9 and 286.2 eV were identified from the XPS spectra of MIP-$C_3N_4$ (Figure 1c), corresponding to two unique chemical bonds from imprinted polymer (i.e., O═C—OH from MAA monomer and C−O−C from EGDMA cross-linker, respectively).[48] This proves that the $C_3N_4$ surface was successfully modified with MAA polymer.

The imprinting of guanine was demonstrated through peak identification from the FTIR spectrum (Figure 1d).[49] The FTIR spectrum of guanine shows a broad absorption in the range of 3000 to 3300 $cm^{-1}$ corresponding to OH group vibrations. Another four peaks at 2906, 1692, 1563, and 1373 $cm^{-1}$ were also identified from the spectra of guanine, respectively, representing C−H stretch, N−H stretch, C═C stretch, and the C−H deformation vibrations. The two absorption peaks at 1120 and 952 $cm^{-1}$ are assigned to C−C stretching vibrations.[49] These specific peaks from guanine were identified from FTIR spectra of as-obtained MIP-$C_3N_4$


https://dx.doi.org/10.1021/acs.est.9b06926
Environ. Sci. Technol. 2020, 54, 4621−4630

before acid washing, indicating that guanine molecules were imprinted into the MAA polymer matrix. As expected, the guanine adsorption peak at 1692 $cm^{-1}$ was prominent before (but barely present after) the polymer was washed with HCl, and both MIP-$C_3N_4$ and NIP-$C_3N_4$ had similar FTIR spectra because of similar surface functional groups. This corroborates that guanine was imprinted into the MAA polymer matrix and removed by subsequent acid washing.

The crystal structure and composition of supporting $C_3N_4$ was analyzed by its XRD pattern (Figure S3). Two major peaks were identified at 27.3° (002) and 13.0° (100), corresponding to the peak of interplanar aromatic stacking and lattice planes parallel to the *c*-axis.[50] Carbon nitride after edge oxidation ($C_3N_4$−COOH) was also characterized by XRD to reveal any possible change on the CN skeleton (Figure S3). Although treatment with $KMnO_4$ could degrade the CN skeleton,[51,52] we used relatively mild conditions that are not conducive to depolymerization, which was corroborated by the XRD diffractogram (Figure S3). Both $C_3N_4$ and $C_3N_4$−COOH showed a similar peak at 13° in the XRD diffraction patterns, indicating that depolymerization of the CN skeleton did not occur. The BET surface area was 85.4 $m^2/g$ for $C_3N_4$, 61.2 $m^2/g$ for MIP-$C_3N_4$, and 60.5 $m^2/g$ for NIP-$C_3N_4$ (Table S2), which is within the reported range for $C_3N_4$ (30−100 $m^2/g$).[53−56]

The Raman spectrum indicates that the MIP coating did not change the characteristic peak of $C_3N_4$ at 1385 $cm^{-1}$ (G-band) and 1565 $cm^{-1}$ (D-band) (Figure S4). Although we observed a blue shift from the UV−vis spectrum compared to bare $C_3N_4$ (Figure S5), this shift was identical for both MIP-$C_3N_4$ and NIP-$C_3N_4$ photocatalysts, indicating that molecular imprinting did not change optical properties. The extent of surface modification was optimized through controllable oxidation of $C_3N_4$ and coating with various amounts of MIP polymer. Four kinds of MIP-$C_3N_4$ with different MIP content were synthesized and characterized by FTIR analysis. Identical functional groups were identified from the FTIR spectrum (Figure S6). Detailed surface functional groups were investigated by XPS, and their MIP content was assessed by the relative abundance of O═C—OH and O−C−O representing MAA monomer and EGDMA cross-linker, respectively (Table S3).[48] Although $C_3N_4$ treatment with $KMnO_4$ could introduce oxygen-containing groups that confound the estimation of the extent of coating per O═C—OH and O−C−O abundance, XPS characterization of $C_3N_4$ after substitution of the introduced carboxylic groups with vinyl groups showed the absence of oxygen-containing groups (Figure S7), which validates our estimation approach.

ARG adsorption is positively correlated with MIP content, whereas eARG photocatalytic degradation activity exhibited a bell-shaped pattern as a function of polymer content (Figure 2). Specifically, photocatalytic degradation increased with polymer content (up to 18.6%) as eARG adsorption near photocatalytic sites enhanced treatment efficiency. However, further coating with this nonphotoactive polymer had a detrimental effect on eARG degradation efficiency, apparently due to occlusion of photocatalytic sites on the $C_3N_4$ surface by excess polymer, which would hinder light penetration and photoexcitation. Therefore, care should be taken when optimizing the polymer content to achieve higher photocatalytic treatment efficiency. The MIP-$C_3N_4$ formulation with the highest photoactivity (corresponding to 18.6% relative abundance of O═C—OH) was adopted for the subsequent experiments.

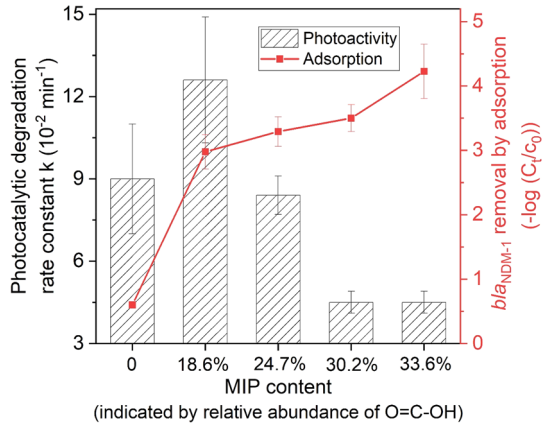


**Figure 2.** Influence of surface coating (molecularly-imprinted polymer) on $bla_{NDM-1}$ adsorption and photocatalytic degradation in DI water. Increasing the content of MIP enhances adsorption of $bla_{NDM-1}$ but deteriorates photocatalytic degradation efficiency. Error bars represent ±1 standard deviation from the mean of triplicate measurements.

**ARGs Removal by MIP-$C_3N_4$ Resists Interference by Background Compounds in Secondary Effluent That Scavenge ROS.** Wastewater constituents can deteriorate the activity of catalyst in two ways: (1) compete with the target pollutant (e.g., $bla_{NDM-1}$) for adsorption sites on the catalyst surface and (2) scavenge ROS that could otherwise be used to degrade the pollutant. Molecular imprinting significantly enhanced selective $bla_{NDM-1}$ adsorption and photocatalytic degradation in the presence of interfering compounds (Figure 3). Specifically, adsorption sites on NIP-$C_3N_4$ were occupied by competing compounds (i.e., peptone, sucrose, humic acid, or other organics in secondary effluent), resulting in 86% to 96% loss of $bla_{NDM-1}$ adsorption at equilibrium (Figure 3a). In contrast, MIP-$C_3N_4$ maintained its high adsorption capacity (i.e., 95% and 98% of the uninhibited value) in the presence of peptone and sucrose, respectively. Adsorption of $bla_{NDM-1}$ by MIP-$C_3N_4$ was inhibited to a greater extent by humic acids (i.e., 58.5% of the uninhibited value) and secondary effluent (i.e., 90.2% of the uninhibited value) but still significantly outperformed NIP-$C_3N_4$ (Figure 3a).

MIP-$C_3N_4$ was highly resistant to interference by background constituents, showing no apparent loss of photocatalytic degradation efficiency toward $bla_{NDM-1}$ (Figure 3b). Only a slight decrease in the first-order degradation rate constant *k* (Table S4) was observed in the presence of the competing organic compounds or secondary effluent (from 0.126 ± 0.023 to 0.111 ± 0.028 $min^{-1}$) (Figure 3b). Photocatalytic degradation of $bla_{NDM-1}$ in secondary effluent was 37 times faster with MIP-$C_3N_4$ (0.111 ± 0.028 $min^{-1}$) than with NIP-$C_3N_4$ (0.003 ± 0.003 $min^{-1}$), highlighting the benefits of molecular imprinting. The lack of ARG removal by photolysis in light-only experiments or in dark controls (after ARG adsorption sites on the MIP-$C_3N_4$ photocatalyst had been saturated) corroborates that photocatalysis was responsible for ARG degradation (Figure S8).

Note that the benefits of molecular imprinting were not observed in DI water, where MIP-$C_3N_4$ and NIP-$C_3N_4$ had similar DNA adsorption capacity based on Langmuir isotherms (Figure S9) (i.e., (4.32 ± 0.06) × $10^{10}$ copies/mg for MIP-


https://dx.doi.org/10.1021/acs.est.9b06926
Environ. Sci. Technol. 2020, 54, 4621−4630

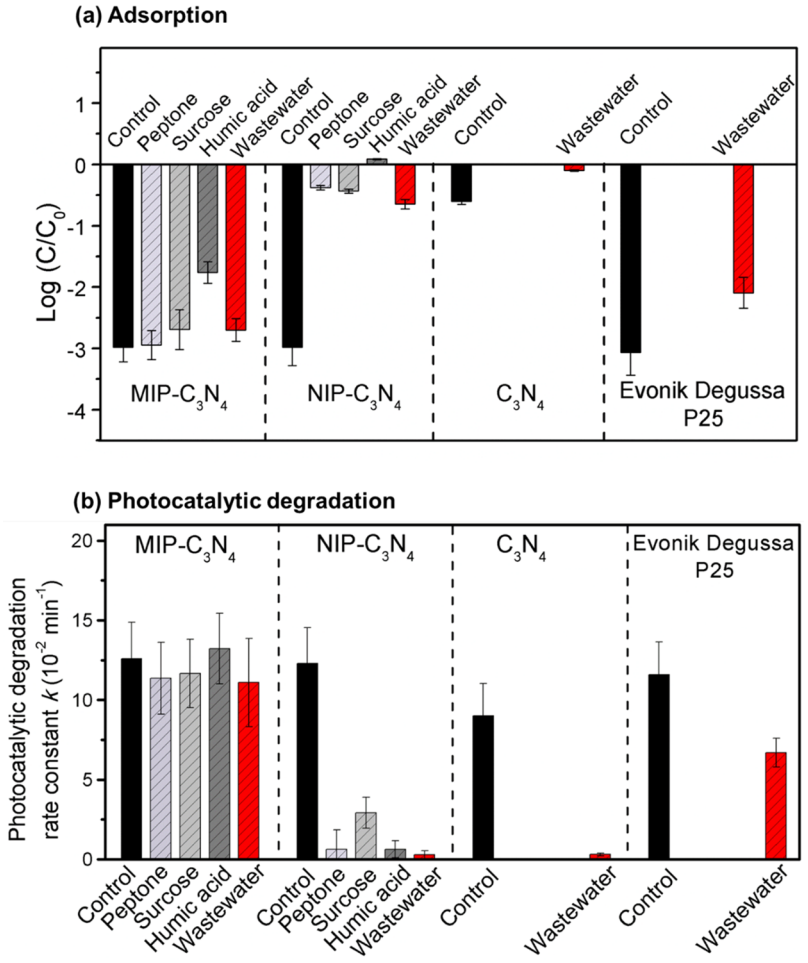


**Figure 3.** Molecular imprinting of guanine on $C_3N_4$ enhances photocatalytic ARG degradation in the presence of various common organic compounds (UVA 365 nm, $3.64 \times 10^{-6}$ Einstein/L·s). Adsorption (a) and photocatalytic degradation (b) of $bla_{NDM-1}$ by MIP-$C_3N_4$ or NIP-$C_3N_4$ in DI water (control) and in the presence of peptone (50 mg/L), sucrose (50 mg/L), humic acid (10 mg/L), or wastewater secondary effluent (TOC = 16.1 mg/L). Results are benchmarked against bare $C_3N_4$ and $TiO_2$ (Evonik Degussa P25) in DI water or secondary effluent.

$C_3N_4$ and $(4.11 \pm 0.03) \times 10^{10}$ copies/mg for NIP-$C_3N_4$). Apparently, DNA adsorbs in a nonspecific manner onto the MAA polymer used for edge modification (i.e., MAA is rich in carboxylic acid groups that can adsorb DNA by hydrogen bonding). Both MIP-$C_3N_4$ and NIP-$C_3N_4$ also efficiently degraded $bla_{NDM-1}$ in DI water without interfering compounds, achieving 3-log removal of $bla_{NDM-1}$ within 1 h with 0.5 mg/mL catalysts.

The incorporation of guanine imprinted polymer provides specific sites for $bla_{NDM-1}$ adsorption and, therefore, mitigates interference by competing background constituents, which is a critical limitation for photocatalytic treatment of ARGs.[16] These sites can selectively adsorb and concentrate DNA (including $bla_{NDM-1}$) on the MIP-$C_3N_4$ surface where heterogeneous photocatalysis occurs. Thus, the photogenerated ROS was more likely to oxidize absorbed $bla_{NDM-1}$ instead of being scavenged by background constituents. The preferential photocatalytic removal of guanine-containing compound by MIP-$C_3N_4$ was corroborated by tests with oligonucleotides having different guanine content (Figure S10). Adsorption and photocatalytic degradation tests showed (as expected) that MIP-$C_3N_4$ preferentially degrades DNA with higher guanine content, regardless of what the DNA codes for (e.g., antibiotic resistance). Since guanine is a common constituent of DNA (and thus ARGs), this approach should also efficiently degrade other eARGs besides $bla_{NDM-1}$.

Photocatalytic performance of MIP-$C_3N_4$ was also benchmarked against a commercially available photocatalyst (Evonik Degussa P25) and bare $C_3N_4$ in secondary effluent (Figure 3). Photocatalytic degradation of $bla_{NDM-1}$ by P25 and bare $C_3N_4$ was significantly inhibited in secondary effluent compared to that in DI water ($0.116 \pm 0.007$ versus $0.067 \pm 0.009$ $min^{-1}$ and $0.090 \pm 0.020$ versus $0.003 \pm 0.001$ $min^{-1}$, respectively). In contrast, MIP-$C_3N_4$ was less susceptible to inhibition in secondary effluent, exhibiting a photocatalytic degradation rate constant ($0.111 \pm 0.028$ $min^{-1}$), which is 1.7 times higher than with P25 and 37-fold higher than with bare $C_3N_4$.

**Photogenerated $h^+$ Plays a Key Role during ARGs "Trap and Zap" Degradation by MIP-$C_3N_4$.** The incorporation of MIP resulted in a $h^+$-dominant pathway of photocatalytic degradation of $bla_{NDM-1}$, which differs from unmodified NIP-$C_3N_4$ where free radicals (i.e., ·OH and $O_2^-$) were the preeminent oxidizers. The degradation of $bla_{NDM-1}$ in the presence of ROS and $h^+$ scavengers was investigated to gain further insight into the photocatalytic degradation mechanisms. Five common photogenerated reactive species (i.e., $h^+$, ·OH, $^1O_2$, $O_2^-$, and $H_2O_2$) were evaluated in terms of their contribution to $bla_{NDM-1}$ degradation. The results of scavenging tests indicate that $h^+$ plays the most important role


https://dx.doi.org/10.1021/acs.est.9b06926
Environ. Sci. Technol. 2020, 54, 4621−4630

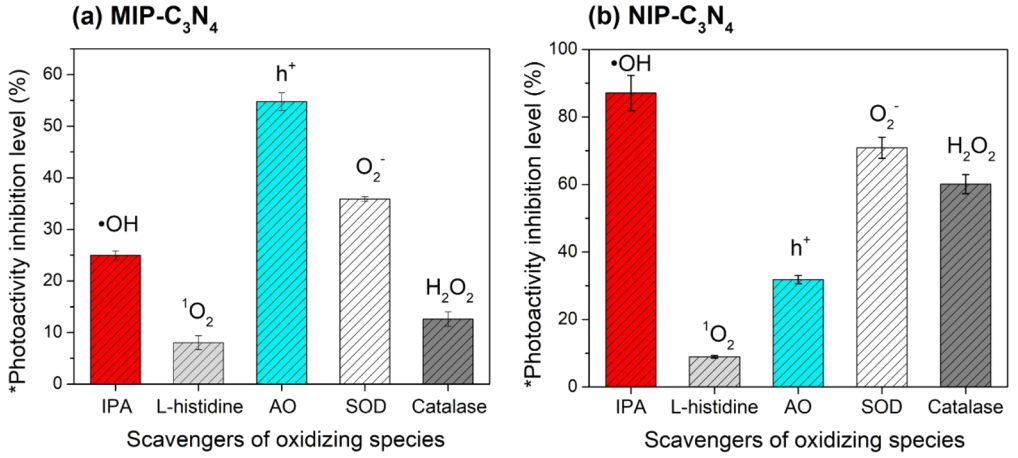


**Figure 4.** Importance of different reactive species in $bla_{NDM-1}$ removal by UVA (365 nm, $3.64 \times 10^{-6}$ Einstein/L·s) irradiated (a) MIP-$C_3N_4$ or (b) NIP-$C_3N_4$, reflected by the photocatalytic inhibition level. The scavengers utilized were 1 mM isopropanol (IPA) for hydroxyl radicals, 1 mM L-histidine for $^1O_2$, 10 mM ammonium oxalate (AO) for electron holes, 50 kU/L superoxide dismutase (SOD) for superoxide, and 200 U/mL catalase for $H_2O_2$.[44,53] (*Photoactivity inhibition level = $(1 \times k_{scavenger}/k_{control}) \times 100\%$).

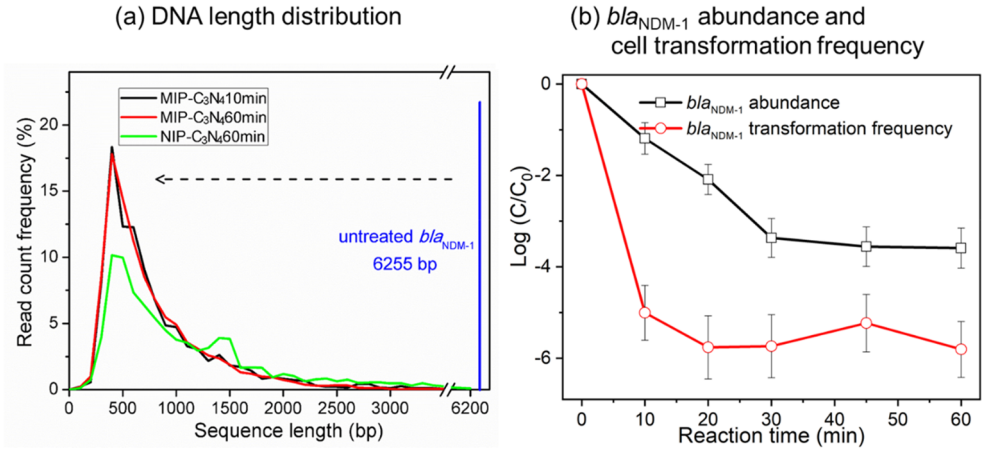


**Figure 5.** Fragmentation of $bla_{NDM-1}$ during photocatalytic treatment by MIP-$C_3N_4$ (UVA of 365 nm, $3.64 \times 10^{-6}$ Einstein/L·s). (a) The DNA length distribution of the $bla_{NDM-1}$ sample after photocatalytic treatment by MIP-$C_3N_4$ (10 and 60 min) and NIP-$C_3N_4$ (60 min). (b) The change of $bla_{NDM-1}$ abundance and transformation frequency (normalized by untreated $bla_{NDM-1}$) treated by MIP-$C_3N_4$ as photocatalyst for various treatment durations.

in the MIP-$C_3N_4$ catalytic system, whereas ·OH and $O_2^-$ are more important for $bla_{NDM-1}$ degradation with NIP-$C_3N_4$ (Figure 4). The $h^+$ on the catalyst surface is an important oxidative species ($E_0$ = 1.5 eV),[57] but unlike ROS, it cannot diffuse into the bulk solution.[44] Therefore, degradation of $bla_{NDM-1}$ that is partially adsorbed to the MIP (on the edges of $C_3N_4$) occurs mainly on the bare photocatalyst surface. MIP would anchor $bla_{NDM-1}$ close to the bare catalyst surface through specific binding to guanine bases. The photogenerated $h^+$, therefore, can attack adsorbed $bla_{NDM-1}$. The ESR spectrum corroborated the production of ·OH by both MIP-$C_3N_4$ and NIP-$C_3N_4$ during UVA irradiation (Figure S11), and its signal was significantly inhibited after adding the ·OH scavenger (IPA) as expected.

MIP-$C_3N_4$ can selectively entrap $bla_{NDM-1}$ owing to its specific binding cavities left by template guanine molecules. These binding cavities help concentrate $bla_{NDM-1}$ on the $C_3N_4$ surface, which facilitates $bla_{NDM-1}$ degradation by a "trap-and-zap" strategy where degradation is mediated by photogenerated $h^+$. In contrast, due to the lack of specific surface trapping, insufficient affinity of $bla_{NDM-1}$ for the NIP-$C_3N_4$ surface does not favor direct contact, and $bla_{NDM-1}$ degradation is primarily mediated by the free radicals (·OH and $O_2^-$) that diffuse away from the photocatalytic sites.

**Extensive Fragmentation by MIP-$C_3N_4$ Inactivates ARGs More Effectively.** MIP-$C_3N_4$ can catalyze the degradation of ARGs to shorter DNA fragments and further to small molecules, eliminating the risk of ARG repair by transformed bacteria in receiving water systems, which is a major limitation for UV disinfection and chlorination.[28,58,59] The chain length distribution of resistance plasmid pET-29a(+) (harboring $bla_{NDM-1}$) (6255 bp) after treatment was determined by nanopore sequencing (Figure 5a). After treatment by MIP-$C_3N_4$ for 10 min, the plasmids were fragmented (7490 fragments) with an average length of 867.5 bp (Table S5). Though only a minor change was observed for the average DNA length (829.4 bp) after extended treatment for 60 min, the counts of total DNA fragments decreased significantly to 1794 (Table S5), indicating an extended breakdown of the DNA fragments to smaller undetected molecules. This sequential fragmentation process was verified by the UV−vis absorbance spectrum of treated $bla_{NDM-1}$. The


https://dx.doi.org/10.1021/acs.est.9b06926
Environ. Sci. Technol. 2020, 54, 4621−4630

absorbance peak of treated $bla_{NDM-1}$ blue-shifted from 260 to 245 nm during the photocatalytic treatment (Figure S12), resulting from the generation of micromolecules.[60,61] In contrast, NIP-$C_3N_4$ was less efficient in fragmenting $bla_{NDM-1}$, yielding 5371 fragments with average length of 2675 bp after 60 min of treatment (Figure 5a, Table S5). This demonstrates that molecular imprinting with guanine endowed $C_3N_4$ with superior capability to mitigate antibiotic resistance propagation.

Fragmentation significantly decreased the transformation potential of $bla_{NDM-1}$. The decrease of transformation frequency was 1 order of magnitude higher than the decrease in $bla_{NDM-1}$ abundance (Figure 5b), and no viable transformed bacteria were observed after exposure to treated $bla_{NDM-1}$. The faster deactivation of $bla_{NDM-1}$ reflects fragmentation of plasmid DNA, which cannot endow hosts with resistance even though the monitored amplicons (by qPCR) remain detectable.[5] Moreover, additional ARG damage (e.g., double helix distortion[62] and partial despiralization) may be caused by photocatalytic oxidation, since the melting temperature of treated $bla_{NDM-1}$ decreased from 89.5 to 82.5 °C after treatment (Figure S13). Therefore, MIP-$C_3N_4$ photocatalytic treatment can outperform UV disinfection, which generally does not cleave DNA[28,63] and thus exposes the receiving environment to the risk of ARG reactivation and propagation by transformed hosts.[28,59]

Stability tests demonstrate sustained performance of MIP-$C_3N_4$ for removing ARGs after repeated use. The photoactivity of MIP-$C_3N_4$ shows no significant loss after 10 cycles (2 h/cycle) (Figure 6). The photoactivity of MIP-$C_3N_4$ in

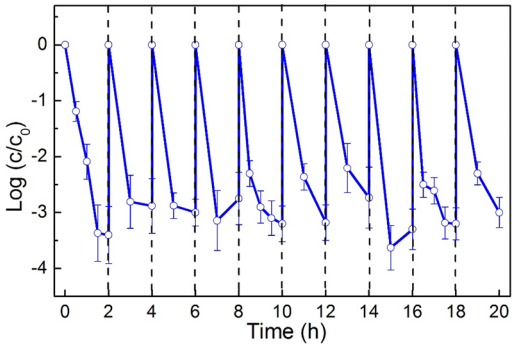


**Figure 6.** Reusability of MIP-$C_3N_4$ was demonstrated by repeated photocatalytic degradation of $bla_{NDM-1}$ in DI water using MIP-$C_3N_4$ recaptured for ten cycles.

secondary effluent also outcompeted P25 $TiO_2$ in reuse tests (Figure S14). Furthermore, no significant changes in morphology and surface functional groups occurred after 10 cycles, on the basis of FTIR spectra (Figure S6) and SEM images (Figure S15).

In summary, a guanine-imprinted polymer coating enhanced the proximity between target extracellular ARGs and photocatalytic sites, which improved the utilization of ROS and electron holes ($h^+$) toward ARG degradation. Accordingly, MIP-$C_3N_4$ efficiently captured and fragmented extracellular ARGs beyond repair. Whereas it is premature to recommend this novel photocatalyst for full-scale application without a comprehensive techno-economic and life cycle analysis, this work demonstrates the potential value of molecular imprinting to enhance the photocatalytic treatment of secondary effluent and mitigate the dissemination of antibiotic resistance with discharge from sewage treatment plants.

## ■ ASSOCIATED CONTENT

### Supporting Information

The Supporting Information is available free of charge at https://pubs.acs.org/doi/10.1021/acs.est.9b06926.

Synthesis of carboxylic carbon nitride, ARG quantification via quantitative PCR, circular map of the plasmid, catalyst surface chemistry analysis, XRD pattern, Raman spectrum, UV−vis spectra, FTIR spectra, XPS spectra, lack of ARG removal in DI water, adsorption kinetics and isotherm, photocatalytic degradation and adsorption removal of oligonucleotides DNA, ESR spectra, melting curve, catalyst reusability in wastewater, SEM images, water quality data, specific surface areas, chemical bond compositions, first-order rate constants, and total read counts and average DNA lengths (PDF)

## ■ AUTHOR INFORMATION


### Corresponding Authors

**Pingfeng Yu** − *Department of Civil and Environmental Engineering, Rice University, Houston, Texas 77005, United States; Nanosystems Engineering Research Center for Nanotechnology Enabled Water Treatment (NEWT), Houston, Texas 77005, United States*; Email: pingfeng.yu@rice.edu

**Pedro J. J. Alvarez** − *Department of Civil and Environmental Engineering, Rice University, Houston, Texas 77005, United States; Nanosystems Engineering Research Center for Nanotechnology Enabled Water Treatment (NEWT), Houston, Texas 77005, United States*; orcid.org/0000-0002-6725-7199; Email: alvarez@rice.edu

### Authors

**Qingbin Yuan** − *College of Environmental Science and Engineering, Nanjing Tech University, Nanjing, Jiangsu 211816, China*

**Danning Zhang** − *Department of Civil and Environmental Engineering, Rice University, Houston, Texas 77005, United States; Nanosystems Engineering Research Center for Nanotechnology Enabled Water Treatment (NEWT), Houston, Texas 77005, United States*

**Ruonan Sun** − *Department of Civil and Environmental Engineering, Rice University, Houston, Texas 77005, United States; Nanosystems Engineering Research Center for Nanotechnology Enabled Water Treatment (NEWT), Houston, Texas 77005, United States*

**Hassan Javed** − *Department of Civil and Environmental Engineering, Rice University, Houston, Texas 77005, United States; Nanosystems Engineering Research Center for Nanotechnology Enabled Water Treatment (NEWT), Houston, Texas 77005, United States*

**Gang Wu** − *Department of Internal Medicine, University of Texas−McGovern Medical School, Houston, Texas 77030, United States*

Complete contact information is available at: https://pubs.acs.org/10.1021/acs.est.9b06926

### Author Contributions

#Q.Y. and D.Z. contributed equally.


### Notes

The authors declare no competing financial interest.



https://dx.doi.org/10.1021/acs.est.9b06926
Environ. Sci. Technol. 2020, 54, 4621−4630

## ■ ACKNOWLEDGMENTS

This study was supported by the NSF ERC on Nanotechnology-Enabled Water Treatment (EEC-1449500), NSF PIRE grant (OISE-1545756), and National Natural Science Foundation of China [grant 51608260]. Q.Y. received financial support from the China Scholarship of Council. We thank Chunzheng Wu, Long Chen, Bo Jiang, and Xiaochuan Huang for their help with the catalyst characterization.

## ■ REFERENCES

(1) O'Neill, J. *Review on antimicrobial resistance: tackling a crisis for the health and wealth of nations*; HM Government: London, 2014.
(2) Luo, Y.; Yang, F.; Mathieu, J.; Mao, D.; Wang, Q.; Alvarez, P. J. J. Proliferation of multidrug-resistant new delhi metallo-$\beta$-lactamase genes in municipal wastewater treatment plants in Northern China. *Environ. Sci. Technol. Lett.* **2014**, *1*, 26−30.
(3) Yuan, Q. B.; Guo, M. T.; Yang, J. Fate of antibiotic resistant bacteria and genes during wastewater chlorination: Implication for antibiotic resistance control. *PLoS One* **2015**, *10* (3), No. e0119403.
(4) Al-Jassim, N.; Ansari, M. I.; Harb, M.; Hong, P.-Y. Removal of bacterial contaminants and antibiotic resistance genes by conventional wastewater treatment processes in Saudi Arabia: Is the treated wastewater safe to reuse for agricultural irrigation? *Water Res.* **2015**, *73*, 277−290.
(5) He, H.; Zhou, P.; Shimabuku, K. K.; Fang, X.; Li, S.; Lee, Y.; Dodd, M. C. Degradation and deactivation of bacterial antibiotic resistance genes during exposure to free chlorine, monochloramine, chlorine dioxide, ozone, ultraviolet light, and hydroxyl radical. *Environ. Sci. Technol.* **2019**, *53* (4), 2013−2026.
(6) Luo, Y.; Mao, D.; Rysz, M.; Zhou, Q.; Zhang, H.; Xu, L.; Alvarez, P. J. J. Trends in antibiotic resistance genes occurrence in the Haihe River, China. *Environ. Sci. Technol.* **2010**, *44* (19), 7220−7225.
(7) Yuan, Q.-B.; Huang, Y.-M.; Wu, W.-B.; Zuo, P.; Hu, N.; Zhou, Y.-Z.; Alvarez, P. J. J. Redistribution of intracellular and extracellular free & adsorbed antibiotic resistance genes through a wastewater treatment plant by an enhanced extracellular DNA extraction method with magnetic beads. *Environ. Int.* **2019**, *131*, 104986.
(8) Guo, M. T.; Yuan, Q. B.; Yang, J. Distinguishing effects of ultraviolet exposure and chlorination on the horizontal transfer of antibiotic resistance genes in municipal wastewater. *Environ. Sci. Technol.* **2015**, *49* (9), 5771−5778.
(9) Guo, M.-T.; Kong, C. Antibiotic resistant bacteria survived from UV disinfection: Safety concerns on genes dissemination. *Chemosphere* **2019**, *224*, 827−832.
(10) Loeb, S. K.; Alvarez, P. J. J.; Brame, J. A.; Cates, E. L.; Choi, W.; Crittenden, J.; Dionysiou, D. D.; Li, Q.; Li-Puma, G.; Quan, X.; Sedlak, D. L.; David Waite, T.; Westerhoff, P.; Kim, J. H. The technology horizon for photocatalytic water treatment: sunrise or sunset? *Environ. Sci. Technol.* **2019**, *53* (6), 2937−2947.
(11) Giannakis, S.; Le, T.-T. M.; Entenza, J. M.; Pulgarin, C. Solar photo-Fenton disinfection of 11 antibiotic-resistant bacteria (ARB) and elimination of representative AR genes. Evidence that antibiotic resistance does not imply resistance to oxidative treatment. *Water Res.* **2018**, *143*, 334−345.
(12) Ong, W.-J.; Tan, L.-L.; Ng, Y. H.; Yong, S.-T.; Chai, S.-P. Graphitic carbon nitride (g-$C_3N_4$)-based photocatalysts for artificial photosynthesis and environmental remediation: are we a step closer to achieving sustainability? *Chem. Rev.* **2016**, *116* (12), 7159−7329.
(13) Teng, Z.; Lv, H.; Wang, C.; Xue, H.; Pang, H.; Wang, G. Bandgap engineering of ultrathin graphene-like carbon nitride nanosheets with controllable oxygenous functionalization. *Carbon* **2017**, *113*, 63−75.
(14) Teng, Z.; Yang, N.; Lv, H.; Wang, S.; Hu, M.; Wang, C.; Wang, D.; Wang, G. Edge-functionalized g-$C_3N_4$ nanosheets as a highly efficient metal-free photocatalyst for safe drinking water. *Chem.* **2019**, *5* (3), 664−680.
(15) Michael-Kordatou, I.; Michael, C.; Duan, X.; He, X.; Dionysiou, D.; Mills, M.; Fatta-Kassinos, D. Dissolved effluent organic matter: characteristics and potential implications in wastewater treatment and reuse applications. *Water Res.* **2015**, *77*, 213−248.
(16) Dunlop, P. S. M.; Ciavola, M.; Rizzo, L.; McDowell, D. A.; Byrne, J. A. Effect of photocatalysis on the transfer of antibiotic resistance genes in urban wastewater. *Catal. Today* **2015**, *240*, 55−60.
(17) BelBruno, J. J. Molecularly imprinted polymers. *Chem. Rev.* **2019**, *119* (1), 94−119.
(18) Kupai, J.; Razali, M.; Buyuktiryaki, S.; Kecili, R.; Szekely, G. Long-term stability and reusability of molecularly imprinted polymers. *Polym. Chem.* **2017**, *8* (4), 666−673.
(19) Rosenberg, E. *It's in your DNA: from discovery to structure, function and role in evolution, cancer and aging*; Academic Press: 2017.
(20) You, M.; Yang, S.; Jiao, F.; Yang, L.-z.; Zhang, F.; He, P.-G. Label-free electrochemical multi-sites recognition of G-rich DNA using multi-walled carbon nanotubes-supported molecularly imprinted polymer with guanine sites of DNA. *Electrochim. Acta* **2016**, *199*, 133−141.
(21) Lofgreen, J. E.; Moudrakovski, I. L.; Ozin, G. A. Molecularly imprinted mesoporous organosilica. *ACS Nano* **2011**, *5* (3), 2277−2287.
(22) Chen, L.; Wang, X.; Lu, W.; Wu, X.; Li, J. Molecular imprinting: perspectives and applications. *Chem. Soc. Rev.* **2016**, *45* (8), 2137−2211.
(23) Luo, X.; Deng, F.; Min, L.; Luo, S.; Guo, B.; Zeng, G.; Au, C. Facile one-step synthesis of inorganic-framework molecularly imprinted $TiO_2/WO_3$ nanocomposite and its molecular recognitive photocatalytic degradation of target contaminant. *Environ. Sci. Technol.* **2013**, *47* (13), 7404−7412.
(24) Lee, C.-G.; Javed, H.; Zhang, D.; Kim, J.-H.; Westerhoff, P.; Li, Q.; Alvarez, P. J. J. Porous electrospun fibers embedding $TiO_2$ for Adsorption and photocatalytic degradation of water pollutants. *Environ. Sci. Technol.* **2018**, *52* (7), 4285−4293.
(25) Zhang, D.; Lee, C.; Javed, H.; Yu, P.; Kim, J.-H.; Alvarez, P. J. Easily recoverable, micrometer-sized $TiO_2$ hierarchical spheres decorated with cyclodextrin for enhanced photocatalytic degradation of organic micropollutants. *Environ. Sci. Technol.* **2018**, *52* (21), 12402−12411.
(26) Mell, J. C.; Redfield, R. J. Natural competence and the evolution of DNA uptake specificity. *J. Bacteriol.* **2014**, *196* (8), 1471−83.
(27) Redfield, R. J. Genes for breakfast: the have-your-cake-and-eat-it-too of bacterial transformation. *J. Hered.* **1993**, *84* (5), 400−4.
(28) Chang, P. H.; Juhrend, B.; Olson, T. M.; Marrs, C. F.; Wigginton, K. R. Degradation of extracellular antibiotic resistance genes with $UV_{254}$ treatment. *Environ. Sci. Technol.* **2017**, *51* (11), 6185−6192.
(29) Poepping, C.; Beck, S. E.; Wright, H.; Linden, K. G. Evaluation of DNA damage reversal during medium-pressure UV disinfection. *Water Res.* **2014**, *56*, 181−189.
(30) Yang, F.; Mao, D.; Zhou, H.; Wang, X.; Luo, Y. Propagation of New Delhi Metallo-$\beta$-lactamase genes ($bla_{NDM-1}$) from a wastewater treatment plant to its receiving river. *Environ. Sci. Technol. Lett.* **2016**, *3* (4), 138−143.
(31) Ahammad, Z. S.; Sreekrishnan, T. R.; Hands, C. L.; Knapp, C. W.; Graham, D. W. Increased waterborne $bla_{NDM-1}$ resistance gene abundances associated with seasonal human pilgrimages to the Upper Ganges River. *Environ. Sci. Technol.* **2014**, *48* (5), 3014−20.
(32) Dong, F.; Zhao, Z.; Sun, Y.; Zhang, Y.; Yan, S.; Wu, Z. An advanced semimetal-organic Bi spheres-g-$C_3N_4$ nanohybrid with SPR-enhanced visible-light photocatalytic performance for NO purification. *Environ. Sci. Technol.* **2015**, *49* (20), 12432−12440.
(33) Wang, W.; Yu, J. C.; Xia, D.; Wong, P. K.; Li, Y. Graphene and g-$C_3N_4$ nanosheets cowrapped elemental $\alpha$-sulfur as a novel metal-free heterojunction photocatalyst for bacterial inactivation under visible-light. *Environ. Sci. Technol.* **2013**, *47* (15), 8724−8732.
(34) Zhao, H.; Yu, H.; Quan, X.; Chen, S.; Zhao, H.; Wang, H. Atomic single layer graphitic-$C_3N_4$: fabrication and its high photocatalytic performance under visible light irradiation. *RSC Adv.* **2014**, *4* (2), 624−628.


https://dx.doi.org/10.1021/acs.est.9b06926
*Environ. Sci. Technol.* 2020, 54, 4621−4630

(35) Cheng, F.; Wang, H.; Dong, X. The amphoteric properties of g-$C_3N_4$ nanosheets and fabrication of their relevant heterostructure photocatalysts by an electrostatic re-assembly route. *Chem. Commun.* **2015**, *51* (33), 7176−7179.
(36) Shen, X.; Huang, C.; Shinde, S.; Switnicka-Plak, M.; Cormack, P. A.; Sellergren, B. Reflux precipitation polymerization: a new synthetic insight in molecular imprinting at high temperature. *RSC Adv.* **2016**, *6* (85), 81491−81499.
(37) Zhang, W.; Li, Y.; Wang, Q.; Wang, C.; Wang, P.; Mao, K. Performance evaluation and application of surface-molecular-imprinted polymer-modified $TiO_2$ nanotubes for the removal of estrogenic chemicals from secondary effluents. *Environ. Sci. Pollut. Res.* **2013**, *20* (3), 1431−1440.
(38) Moreira, N. F.; Narciso-da-Rocha, C.; Polo-López, M. I.; Pastrana-Martínez, L. M.; Faria, J. L.; Manaia, C. M.; Fernández-Ibáñez, P.; Nunes, O. C.; Silva, A. M. Solar treatment ($H_2O_2$, $TiO_2$-P25 and GO-$TiO_2$ photocatalysis, photo-Fenton) of organic micro-pollutants, human pathogen indicators, antibiotic resistant bacteria and related genes in urban wastewater. *Water Res.* **2018**, *135*, 195−206.
(39) Zhang, Y.; Gan, H.; Zhang, G. A novel mixed-phase $TiO_2$/kaolinite composites and their photocatalytic activity for degradation of organic contaminants. *Chem. Eng. J.* **2011**, *172* (2−3), 936−943.
(40) Yang, Y.; Zhang, G.; Xu, W. Facile synthesis and photocatalytic properties of Ag-AgCl-$TiO_2$/rectorite composite. *J. Colloid Interface Sci.* **2012**, *376* (1), 217−223.
(41) Kim, J. R.; Premier, G. C.; Hawkes, F. R.; Rodríguez, J.; Dinsdale, R. M.; Guwy, A. J. Modular tubular microbial fuel cells for energy recovery during sucrose wastewater treatment at low organic loading rate. *Bioresour. Technol.* **2010**, *101* (4), 1190−1198.
(42) Kositzi, M.; Poulios, I.; Malato, S.; Caceres, J.; Campos, A. Solar photocatalytic treatment of synthetic municipal wastewater. *Water Res.* **2004**, *38* (5), 1147−1154.
(43) Hsu, H.; Sedlak, D. L. Strong Hg(II) complexation in municipal wastewater effluent and surface waters. *Environ. Sci. Technol.* **2003**, *37* (12), 2743−2749.
(44) Nosaka, Y.; Nosaka, A. Y. Generation and detection of reactive oxygen species in photocatalysis. *Chem. Rev.* **2017**, *117* (17), 11302−11336.
(45) Yu, P. F.; Mathieu, J.; Lu, G. W.; Gabiatti, N.; Alvarez, P. J. Control of antibiotic-resistant bacteria in activated sludge using polyvalent phages in conjunction with a production host. *Environ. Sci. Technol. Lett.* **2017**, *4* (4), 137−142.
(46) Pak, G.; Salcedo, D. E.; Lee, H.; Oh, J.; Maeng, S. K.; Song, K. G.; Hong, S. W.; Kim, H.-C.; Chandran, K.; Kim, S. Comparison of antibiotic resistance removal efficiencies using ozone disinfection under different pH and suspended solids and humic substance concentrations. *Environ. Sci. Technol.* **2016**, *50* (14), 7590−7600.
(47) Chong, M. N.; Jin, B.; Chow, C. W.; Saint, C. Recent developments in photocatalytic water treatment technology: a review. *Water Res.* **2010**, *44* (10), 2997−3027.
(48) Dietrich, P. M.; Hennig, A.; Holzweber, M.; Thiele, T.; Borcherding, H.; Lippitz, A.; Schedler, U.; Resch-Genger, U.; Unger, W. E. Surface analytical study of poly-(acrylic acid)-grafted microparticles (beads): characterization, chemical derivatization, and quantification of surface carboxyl groups. *J. Phys. Chem. C* **2014**, *118* (35), 20393−20404.
(49) Chandraboss, V.; Karthikeyan, B.; Senthilvelan, S. Experimental and first-principles investigation of the adsorption and entrapping of guanine with $SiO_2$ clusters of sol-gel silicate material for understanding DNA photodamage. *Phys. Chem. Chem. Phys.* **2015**, *17* (18), 12100−12114.
(50) Lu, X.; Xu, K.; Chen, P.; Jia, K.; Liu, S.; Wu, C. Facile one step method realizing scalable production of g-$C_3N_4$ nanosheets and study of their photocatalytic $H_2$ evolution activity. *J. Mater. Chem. A* **2014**, *2* (44), 18924−18928.
(51) Niu, P.; Zhang, L.; Liu, G.; Cheng, H.-M. Graphene-like carbon nitride nanosheets for improved photocatalytic activities. *Adv. Funct. Mater.* **2012**, *22* (22), 4763−4770.
(52) Zhang, J.; Zhang, M.; Lin, L.; Wang, X. Sol processing of conjugated carbon nitride powders for thin-film fabrication. *Angew. Chem., Int. Ed.* **2015**, *54* (21), 6297−6301.
(53) Zheng, Q.; Durkin, D. P.; Elenewski, J. E.; Sun, Y.; Banek, N. A.; Hua, L.; Chen, H.; Wagner, M. J.; Zhang, W.; Shuai, D. Visible-light-responsive graphitic carbon nitride: rational design and photocatalytic applications for water treatment. *Environ. Sci. Technol.* **2016**, *50* (23), 12938−12948.
(54) Xu, H.; Yan, J.; She, X.; Xu, L.; Xia, J.; Xu, Y.; Song, Y.; Huang, L.; Li, H. Graphene-analogue carbon nitride: novel exfoliation synthesis and its application in photocatalysis and photoelectrochemical selective detection of trace amount of $Cu^{2+}$. *Nanoscale* **2014**, *6* (3), 1406−1415.
(55) He, Y.; Zhang, L.; Teng, B.; Fan, M. New application of Z-scheme $Ag_3PO_4$/g-$C_3N_4$ composite in converting $CO_2$ to fuel. *Environ. Sci. Technol.* **2015**, *49* (1), 649−656.
(56) Wu, X.; Lu, C.; Liu, J.; Song, S.; Sun, C. Constructing efficient solar light photocatalytic system with Ag-introduced carbon nitride for organic pollutant elimination. *Appl. Catal., B* **2017**, *217*, 232−240.
(57) Kumar, S.; Karthikeyan, S.; Lee, A. F. G-$C_3N_4$-based nanomaterials for visible light-driven photocatalysis. *Catalysts* **2018**, *8* (2), 74.
(58) Wu, M. S.; Xu, X. Inactivation of antibiotic-resistant bacteria by chlorine dioxide in soil and shifts in community composition. *RSC Adv.* **2019**, *9* (12), 6526−6532.
(59) Bucher, D. B.; Kufner, C. L.; Schlueter, A.; Carell, T.; Zinth, W. UV-induced charge transfer states in DNA promote sequence selective self-repair. *J. Am. Chem. Soc.* **2016**, *138* (1), 186−190.
(60) Eshkourfu, R.; Cobeljic, B.; Vujcic, M.; Turel, I.; Pevec, A.; Sepcic, K.; Zec, M.; Radulovic, S.; Srdic-Radic, T.; Mitic, D.; Andjelkovic, K.; Sladic, D. Synthesis, characterization, cytotoxic activity and DNA binding properties of the novel dinuclear cobalt(III) complex with the condensation product of 2-acetylpyridine and malonic acid dihydrazide. *J. Inorg. Biochem.* **2011**, *105* (9), 1196−203.
(61) Schmidt, F. Biological macromolecules: UV-visible spectrophotometry. *eLS* **2001**; DOI: 10.1038/npg.els.0003142.
(62) Galyuk, E. N.; Fridman, A. S.; Vorobev, V. I.; Haroutiunian, S. G.; Sargsyan, S. A.; Hauruk, M. M.; Lando, D. Y. Compensation of DNA stabilization and destabilization effects caused by cisplatin is partially disturbed in alkaline medium. *J. Biomol. Struct. Dyn.* **2008**, *25* (4), 407−417.
(63) Peak, J. G.; Peak, M. J. Ultraviolet light induces double-strand breaks in DNA of cultured human p3 cells as measured by neutral filter elution. *Photochem. Photobiol.* **1990**, *52* (2), 387−393.


https://dx.doi.org/10.1021/acs.est.9b06926
*Environ. Sci. Technol.* 2020, 54, 4621−4630